Local Mobility within Villin 14T Probed via Heteronuclear Relaxation Measurements and a Reduced Spectral Density Mapping†

Michelle A. Markus,‡,|| Kwaku T. Dayie,‡ Paul Matsudaira,§ and Gerhard Wagner*,‡

Department of Biological Chemistry and Molecular Pharmacology, Harvard Medical School, and Committee on Higher Degrees in Biophysics, Harvard University, 240 Longwood Avenue, Boston, Massachusetts 02115, and Whitehead Institute for Biomedical Research and Department of Biology, Massachusetts Institute of Technology, Nine Cambridge Center, Cambridge, Massachusetts 02142

Received August 16, 1995; Revised Manuscript Received November 16, 1995⊗

ABSTRACT: Villin 14T, a representative domain from the actin severing and bundling protein villin, binds calcium ions and actin monomers. To begin to understand the contributions of mobility to the villin−calcium and villin−actin interactions, relaxation rates for magnetization involving the amide nitrogens and protons have been measured for ^{15}N-labeled villin 14T in solution. Although we have measured the complete set of rates required for a full spectral density map, difficulties in the accurate measurement of relaxation rates for antiphase coherence and two-spin order led us to consider a reduced mapping formalism. From the reduced spectral density map, a model-free analysis, or directly from the measured $N_{x,y}$ relaxation rates, local variations in mobility along the backbone of villin 14T have been revealed. Fast motions are evident not only at the amino and carboxyl termini but also in the turn between strands β4 and β5 of the central β-sheet and in the turn between helix α3 and strand β7. Slower motions are suggested for the turn between strands β2 and β3. Motions on the microsecond to millisecond time scale have been probed directly by examining the dependence of the proton transverse relaxation rate on the spin-locking field strength. Leu^{11} shows a strong dependence on field strength, implying conformational exchange with a time constant of 125 ± 69 μs. The backbone at the actin-binding interface appears to be rather rigid.

Villin 14T, spanning 126 amino acids (14 kDa),[1] is the first of six repeated domains in the actin severing and bundling protein, villin (Bazari et al., 1988). Alone, this domain binds to actin monomers in the presence of calcium (Janmey & Matsudaira, 1988). Two calcium binding sites have been identified within villin 14T, and their dissociation constants have been measured (Markus et al., 1994a). The solution structure of villin 14T, taken together with the crystal structure of the analogous domain from the actin severing protein gelsolin in complex with an actin monomer (McLaughlin et al., 1993), reveals the structure of the actin-binding site. However, structural complementarity is only one possibility for protein−protein interactions. Induced fit in otherwise flexible regions is another alternative. To understand the interactions of villin 14T with calcium and actin in more detail, it is important to probe the mobility in solution for sites within villin 14T.

The relaxation of nonequilibrium magnetization in an external field is sensitive to the motions of the magnetic nuclei. The random fluctuations associated with motion couple to the internal energy levels of the magnetic spin systems and provide a mechanism for returning the systems to thermal equilibrium. Though relaxation has been of interest since the first observations of nuclear magnetic resonance (Bloch, 1946; Bloembergen et al., 1948; Redfield, 1965), recent developments using indirect detection of insensitive nuclei in two-dimensional experiments (Nirmala & Wagner, 1988; Nirmala & Wagner, 1989) and taking advantage of the availability of labeled samples (Sklenár et al., 1987; Kay et al., 1989) make relaxation a powerful tool for the study of mobility at specific sites within proteins.

Relaxation data are typically interpreted with the aid of a model, describing either the motions themselves or the analytical form of the spectral density functions. Among the least restrictive ways of analyzing relaxation data is the model-free approach (Lipari & Szabo, 1982a,b), which assumes that the spectral density function is the sum of two Lorentzian functions. This model features three parameters, S^2, the generalized order parameter, τ_m, the overall tumbling correlation time for the molecule, and τ_e, the correlation time for internal motions, which can be fit on the basis of two relaxation rates and NOE enhancement data. Extensions to this approach, adding parameters for additional motions on another time scale (Clore et al., 1990a) or for exchange contributions to transverse relaxation, have been proposed for several proteins where the original model-free approach does not fit the data well (Clore et al., 1990b).

More recently, the motional information contained within the relaxation rates has been extracted without regard to any model by mapping the power spectral density functions (Peng & Wagner, 1992a,b). In this technique, no a priori assumptions have to be made about the analytical form of the spectral density function. This is in contrast to the model-free approach where the relaxation rates are fitted to the parameters defining the spectral density function as a sum of two or three Lorentzians. However, after spectral density values have been obtained via the mapping technique, they

† This research has been supported by the National Institutes of Health, through Grant GM38608, and by the National Science Foundation, through Grant MCB9316938, to G.W.

‡ Harvard Medical School.

|| Present address: National Institute of Dental Research, 30 Convent Drive, Bethesda, MD 20892-4320.

§ Whitehead Institute for Biomedical Research.

⊗ Abstract published in *Advance ACS Abstracts,* January 15, 1996.

[1] Abbreviations: HSQC, heteronuclear single-quantum coherence; INEPT, insensitive nuclei enhanced by polarization transfer; NMR, nuclear magnetic resonance; NOE, nuclear Overhauser effect; NOESY, nuclear Overhauser effect spectroscopy; RMSD, root mean square deviation; villin 14T, residues 1−126 from the chicken epithelial sequence of the actin-binding protein villin.

0006-2960/96/0435-1722$12.00/0

can be fitted to any functional forms of spectral density functions, such as sums of Lorentzians analogous to those proposed in the model-free approach. The method of spectral density mapping has first been applied to the 8 kDa proteinase inhibitor eglin *c*. Through measurements of six nitrogen and proton relaxation rates, the power spectral density functions have been mapped. Here we describe similar measurements and efforts to obtain a full spectral density map for the 14 kDa actin-binding domain villin 14T. Inconsistencies in the full spectral density map led us to consider a reduced spectral density map (Wagner, 1994; Farrow et al., 1995; Lefévre et al., 1996), both to interpret the rates in terms of motions and to explore the likely sources of inconsistencies in the full map. The rates have also been interpreted according to the model-free approach and its extensions. Finally, slower motional processes have been probed through the dependence of proton transverse relaxation on spin-locking field strength. The implications for mobility in villin 14T, as well as for calcium and actin binding, are presented below.

MATERIALS AND METHODS

The Sample. ^{15}N-Labeled villin 14T was expressed in *Escherichia coli* grown in minimal medium containing $^{15}NH_4Cl$ as the sole nitrogen source and purified as described (Markus et al., 1994b). The sample concentration is 2.29 mM in 50 mM NaH_2PO_4, 100 mM NaCl, and 0.1 mM NaN_3 at approximately pH 4.13. To reduce the amount of dissolved oxygen in the sample, and thus remove this contribution to relaxation, the sample was sealed under argon.

Description of Pulse Sequences and Parameters. All of the rates and NOE enhancements were measured on a Bruker AMX-500 spectrometer at 298 K. The rate experiments are essentially 2D heteronuclear correlation experiments with appropriate relaxation delays inserted. Magnetization transfers from the protons to the nitrogen and back are accomplished through INEPT.

The rates $R_N(N_z)$, $R_N(N_{x,y})$, $R_{HN}(2H_zN_z)$, and $R_{HN}(2H_zN_{x,y})$, as well as the heteronuclear NOE enhancements, were measured using gradient-enhanced pulse sequences (Dayie & Wagner, 1994). In these experiments, magic-angle pulsed-field gradients are used to suppress the water resonance and to select for the $^{15}N-^1H$ magnetization (Davis et al., 1992). The gradient selection of coherence pathways is combined with detection of both orthogonal components of the in-phase proton magnetization, creating "sensitivity-enhanced" experiments (Palmer et al., 1991; Kay et al., 1992a). These experiments also feature "flip-back" pulses to minimize saturation of the water (Grzesiek & Bax, 1993). For measurements of $R_N(N_{x,y})$ and $R_{NH}(2H_zN_{x,y})$, a spin-locking field is applied during the relaxation delay. Therefore, these rates strictly correspond to $R_N(N_{\rho z})$ and $R_{NH}(2H_zN_{\rho z})$ (Peng et al., 1991). The details of acquisition for villin 14T have been reported (Dayie & Wagner, 1994).

The amide proton longitudinal relaxation rates [$R_H(H_z^N)$] were measured with the pulse sequence described in Peng and Wagner (1992a). The experiment is essentially a 2D version of an ^{15}N HSQC-NOESY, using the NOESY mixing time as the relaxation delay, with ^{15}N chemical shifts along ω_1 and ^{1}H chemical shifts along ω_2. Water suppression is accomplished with presaturation. The details of the proton relaxation experiment have also been presented (Markus et al., 1994c).

The proton rotating frame relaxation rates, $R_H(H_{\rho z})$, were measured with the pulse sequence and parameters described in Dayie and Wagner (1994). The rates were measured at spin-locking field strengths of 3.21, 4.55, 6.02, 8.20, and 11.52 kHz.

Data Processing and Calculation of the Relaxation Rates. Spectra were processed in Felix (Biosym Technologies, San Diego, CA), with multiplication by 60°-shifted sine-squared apodization functions and 4-fold zero-filling in both dimensions. For sensitivity-enhanced data, the echo/antiecho pairs were added and subtracted (with a 90° phase correction) to form complex points in the acquisition dimension, either before processing or within the Felix macro. The data were analyzed as described in Peng and Wagner (1992a). Briefly, peak intensities were measured by integrating cross sections taken along the ^{1}H dimension at the peak maximum. Intensities were fit to single exponential functions via the Levenburg−Marquardt nonlinear least squares method, implemented in PLOT (New Unit Inc., Ithaca, NY). Examples of the fits for residue Ala^{76} have been published (Dayie & Wagner, 1994). Uncertainties in the peak intensities were estimated by repetition of one time point in the relaxation series. These uncertainties were used to estimate uncertainties in the rates due to random errors via Monte Carlo simulations as in Peng and Wagner (1992b).

Spectral Density Mapping Based on the Relaxation Rates. In the quantum mechanical description of relaxation in magnetic spin systems, the Hamiltonian is typically expressed as the product of a "lattice" component and a "spin" component. [See Abragam (1961).] The spin component includes interactions that are constant in time and gives rise to the observed spectrum. The lattice component includes interactions that fluctuate randomly in time, due to motion within the system. This component gives rise to relaxation, which causes broadening of the observed spectrum. The dependence on fluctuations over time is expressed as the power spectral density function, $J(\omega)$. More directly, the spectral density function can be interpreted as the Fourier transform of the correlation function for motions of the H−N amide bond vector. The spectral density depends critically on the motions occurring within the system. The relaxation rates sample the spectral density function at distinct frequencies, as detailed (Abragam, 1961; Peng & Wagner, 1992b; Wagner, 1993):

$$R_N(N_z) = d\{J(\omega_H - \omega_N) + 3J(\omega_N) + 6J(\omega_H + \omega_N)\} + c\{J(\omega_N)\} \quad (1)$$

$$R_N(N_{x,y}) = \frac{d}{2}\{4J(0) + J(\omega_H - \omega_N) + 3J(\omega_N) + 6J(\omega_H) + 6J(\omega_H + \omega_N)\} + c\left\{\frac{2}{3}J(0) + \frac{1}{2}J(\omega_N)\right\} + R_{ex}^N \quad (2)$$

$$R_{HN}(2H_zN_z) = d\{3J(\omega_N) + 3J(\omega_H)\} + c\{J(\omega_N)\} + \varrho_{H^NH^i} \quad (3)$$

$$R_{HN}(2H_zN_{x,y}) = \frac{d}{2}\{4J(0) + J(\omega_H - \omega_N) + 3J(\omega_N) + 6J(\omega_H + \omega_N)\} + c\left\{\frac{2}{3}J(0) + \frac{1}{2}J(\omega_N)\right\} + \varrho_{H^NH^i} + R_{ex}^N \quad (4)$$

with

$$\varrho_{H^NH^i} = \sum_{i=1}^{N} d_{H^i}\{J_{H^NH^i}(0) + 3J_{H^NH^i}(\omega_H) + 6J_{H^NH^i}(2\omega_H)\} \quad (5)$$

In eq 5, the proton Larmor frequencies are assumed to be approximately equal ($\omega_{H^N} = \omega_{H^i}$) such that $J_{H^NH^i}(\omega_{H^N} - \omega_{H^i}) = J(0)$ and $J_{H^NH^i}(\omega_{H^N} + \omega_{H^i}) = J_{H^NH^i}(2\omega_H)$. For selective measurement of proton longitudinal relaxation

$$R_H(H_z^N) = d\{J(\omega_H - \omega_N) + 3J(\omega_H) + 6J(\omega_H + \omega_N)\} + \varrho_{H^NH^i} \quad (6)$$

R_X represents the relaxation rates, as indicated in the text, with X representing the nuclei involved (H, N, or HN). d is the weight of the dipolar interaction between the amide nitrogen and proton, while the d_{H^i} are the weights of the dipolar interactions between the protons. c is the strength of the chemical shift anisotropy. These constants are given by

$$d = \frac{\hbar^2\gamma_H^2\gamma_N^2}{4r_{HN}^6} \qquad d_{H^i} = \frac{\hbar^2\gamma_H^4}{4r_{HNi}^6} \qquad c = \frac{\omega_N^2\Delta_N^2}{3} \quad (7)$$

where $\hbar$ is Planck's constant divided by 2π, γ is the gyromagnetic ratio, r represents the distance between the nuclei involved in the dipolar interaction, and Δ_N is the chemical shift anisotropy for the amide nitrogen, assuming axial symmetry for the chemical shift anisotropy tensor. J represents the spectral density functions, with the corresponding frequency given in parentheses, $\rho_{H^NH^i}$ is the longitudinal proton cross-relaxation rate, and R_{ex}^N is the relaxation of nitrogen magnetization due to exchange processes. The heteronuclear NOE can be related to the rate for cross relaxation between the amide proton and nitrogen and the nitrogen longitudinal relaxation rate as follows:

$$\eta = \frac{I_{sat} - I_{eq}}{I_{eq}} = \frac{\gamma_H}{\gamma_N}\frac{R_N(H_z^N \leftrightarrow N_z)}{R_N(N_z)} \quad (8)$$

where

$$R_{HN}(H_z^N \leftrightarrow N_z) = d\{-J(\omega_H - \omega_N) + 6J(\omega_H + \omega_N)\} \quad (9)$$

Neglecting exchange contributions, the rates in the expressions above depend on only five values of the spectral density function for the amide nitrogen [$J(0)$, $J(\omega_N)$, $J(\omega_H + \omega_N)$, $J(\omega_H)$, and $J(\omega_H - \omega_N)$] and the proton−proton spin−lattice relaxation ($\rho_{H^NH^i}$). Therefore, the expressions given above can be solved for the spectral densities themselves to give a map of the spectral density function at those frequencies (Peng & Wagner, 1992b).

Reduced Spectral Density Map Based on Two Rates and the NOE Enhancement. For proteins, the value of the spectral density at zero frequency [$J(0)$] is relatively large while the values at higher frequencies are orders of magnitude smaller. On the basis of the experimental results for eglin c (Peng & Wagner, 1992b), it is a reasonable approximation to equate the high-frequency values of the spectral density function [$J(\omega_H + \omega_N) = J(\omega_H) = J(\omega_H - \omega_N)$]. In this case, the reduced spectral density can be mapped with the rates $R_N(N_z)$ and $R_N(N_{x,y})$ and the heteronuclear NOE. The expressions for the available components of the spectral density function in terms of these rates are:

$$J_{eff}(0) = \frac{3}{2(3d + c)}\left[-\frac{1}{2}R_N(N_z) + R_N(N_{x,y}) - \frac{3}{5}R_{HN}(H_z^N \leftrightarrow N_z)\right] \quad (10)$$

$$J(\omega_N) = \frac{1}{(3d + c)}\left[R_N(N_z) - \frac{7}{5}R_{HN}(H_z^N \leftrightarrow N_z)\right] \quad (11)$$

$$J(\omega_h) = \frac{1}{5d}R_{HN}(H_z^N \leftrightarrow N_z) \quad (12)$$

with

$$J(\omega_h) = J(\omega_H + \omega_N) = J(\omega_H) = J(\omega_H - \omega_N) \quad (13)$$

The constants are given by eq 7, and the proton−nitrogen cross-relaxation rate is related to the heteronuclear NOE enhancement by eq 8. $J_{eff}(0)$ denotes that, since exchange is not considered explicitly, $J(0)$ includes the exchange contribution from $R_N(N_{x,y})$.

Model-Free Parameters from the Relaxation Rates. To interpret the dynamic information contained in the relaxation rates and the spectral density functions, typically some motional model is invoked. One formalism that makes relatively few assumptions about the details of the motions and introduces relatively few adjustable parameters is the model-free approach (Lipari & Szabo, 1982a,b). In this approach, the spectral density functions are assumed to be the sum of two Lorentzians:

$$J(\omega) = \frac{2}{5}\left(\frac{S^2\tau_m}{1 + \tau_m^2\omega^2} + \frac{(1 - S^2)\tau}{1 + \tau^2\omega^2}\right) \quad (14)$$

with

$$\frac{1}{\tau} = \frac{1}{\tau_m} + \frac{1}{\tau_e}$$

S^2 is a generalized order parameter which provides a measure of the degree of spatial restriction of the motion, τ_m is the correlation time for the tumbling of the molecule, and τ_e is an effective correlation time, which gives some measure of the rate of local motion after the rate of the overall motion is considered through τ_m. Notice that when $S^2 = 1$, the single Lorentzian that results corresponds to the model based on rotational diffusion of a rigid body. This indicates that a completely ordered amide vector only displays motion due to the overall rotation of the molecule. For a completely disordered amide vector, $S^2 = 0$.

In the extended treatment, an additional Lorentzian term is included in the expression for the spectral density function (Clore et al., 1990a):

$$J(\omega) = \frac{2}{5}\left(\frac{S^2\tau_m}{1 + \tau_m^2\omega^2} + \frac{(1 - S_f^2)\tau_f}{1 + \tau_f^2\omega^2} + \frac{(S_f^2 - S^2)\tau_s}{1 + \tau_s^2\omega^2}\right) \quad (15)$$

where S_f^2 is the generalized order parameter for fast internal motions, τ_f is the corresponding correlation time, and τ_s is an additional correlation time for motions on a time scale distinctly slower than τ_f. The measured relaxation rates $R_N(N_z)$ and $R_N(N_{x,y})$ together with the heteronuclear NOE enhancements were fit to spectral densities of the forms in eqs 14 and 15 and to the additional case where the exchange contribution to $R_N(N_{x,y})$ is considered explicitly.

Probing Slower Motions via Spin Locking at Different Field Strengths. The transverse relaxation rate measured with spin locking during the relaxation delay can be influenced by chemical exchange processes with frequencies near the frequency of the spin-locking field. For the case of exchange between two states, A and B, the dependence of the relaxation rate on the spin-locking field is given by (Szyperski et al., 1993)

$$R_X(X_{\varrho z}) = p_A p_B \Delta\Omega^2 \frac{\tau_{ex}}{1 + \tau_{ex}^2 \omega_1^2} + R_X(X_{\varrho_z}^{\infty}) \quad (16)$$

where X is the nucleus under consideration (here the proton relaxation has been examined at different spin-locking fields), p_A is the population of state A and p_B is the population of state B, $\Delta\Omega$ is the difference in chemical shifts between the two states, τ_{ex} is the time constant for the exchange, ω_1 is the spin-locking field strength, and $R_X(X_{\varrho_z}^{\infty})$ is the rate extrapolated to an infinite spin-locking power. To fit the expression, essentially three constants must be considered: $p_A p_B \Delta\Omega \tau_{ex}$, τ_{ex} itself, and $R_X(X_{\varrho_z}^{\infty})$ (Blackledge et al., 1993). Here, eq 16 was fit with the general curve fitting option in KaleidaGraph (Abelbeck Software, Reading, PA), which uses the Levenburg−Marquardt algorithm.

RESULTS

Measured Rates. The set of five rates and the heteronuclear NOE enhancement required for spectral density mapping are shown in Figure 1. For the nitrogen longitudinal relaxation rate [$R_N(N_z)$, Figure 1A], the average value is 1.68 s^{-1} with a range from 0.55 to 2.00 s^{-1}. Notice the small dips in the rates in the turn between strands β4 and β5 and at the carboxyl terminus. These trends are even more pronounced in the transverse relaxation rates [$R_N(N_{x,y})$, Figure 1B]. In addition, there is a dip between helix α3 and strand β7. Noticeably larger values of the transverse relaxation rate are observed for Lys[34] (between strands β2 and β3) and Asn[38] (in strand β3). Large values of the transverse relaxation rate, without corresponding large values for the longitudinal rate, typically reflect conformational exchange. (See eq 2.) The rates for transverse relaxation have an average of 12.13 s^{-1} (range 2.20−15.88 s^{-1}). The two-spin rates, $R_{HN}(2H_zN_z)$ and $R_{HN}(2H_zN_{x,y})$, are displayed in Figure 1C,D. The average values are 11.4 s^{-1} (range 3.87−18.1 s^{-1}) for $R_{HN}(2H_zN_z)$ and 29.0 s^{-1} (range 5.58−47.0 s^{-1}) for $R_{HN}(2H_zN_{x,y})$. The same general trends in the rates are observed, although they are less clear due to contributions from proton-proton relaxation. (See eqs 3 and 4.) The magnitudes of the heteronuclear NOE enhancements are displayed in Figure 1E. The average value is 0.319 with a range from 0.086 to 2.352, where the largest value is observed for the Arg[51] side chain. The enhancement shows larger magnitudes at the very amino terminus (Val[1]), between strands β4 and β5, between helix α3 and strand β7, and at the carboxyl terminus (from Gly[120] forward). The proton longitudinal relaxation rates [$R_H(H_z^N)$] are shown in Figure 1F. The average rate is 7.75 s^{-1} with a range from 3.28 to 11.69 s^{-1}. Even though the proton relaxation includes the additional contribution from proton−proton cross relaxation (eq 6), the same trends are apparent, namely, decreased rates in the turn between strands β4 and β5, between α3 and β7, and at the carboxyl terminus.

Notice that, in addition to the rates for the backbone N−H groups, the graphs show the rates for the side chain N−H groups of tryptophan and arginine at the far right. Trp[21] and Trp[64] are in the central β-sheet of villin 14T, with Trp[21] packing into helices α1 and α2 on one side of the sheet and Trp[64] packing into helix α3 across the other side of the sheet. In general, the rates for the tryptophan groups follow trends similar to those for the well-defined secondary structure in the domain. Arg[22] is on the same side of the central β-sheet as Trp[64] and also tends to follow the trends of the well-defined secondary structure. However, Arg[51], Arg[96], and Arg[107] follow trends more similar to the extreme ends of the peptide chain. Arg[51] is near the end of strand β4, Arg[96] is in strand β6 at the edge of the central β-sheet, and Arg[107] is in helix α3. These three side chains are on the surface of the protein, exposed to solvent.

Numerical Problems in the Full Spectral Density Mapping. The full spectral density mapping produces unphysical negative values for the high-frequency components [$J(\omega_H + \omega_N)$, $J(\omega_H)$, and $J(\omega_H - \omega_N)$] in villin 14T. One source of the negative spectral densities at high frequencies is probably the limitation on the dynamic range in the experiments. The relaxation rates for nitrogen transverse magnetization, antiphase magnetization, and two-spin order are much larger than the rates for nitrogen and proton longitudinal magnetization, which in turn are much larger than the heteronuclear NOE enhancement. In the expressions for the high-frequency components of the spectral density function (Peng & Wagner, 1992b), large rates are added and subtracted to produce tiny values. Even a small percentage error in one of these rates is sufficient to cause unphysical values for the very small high-frequency spectral densities. $J(0)$ and $J(\omega_N)$ are less affected simply because they are larger. Negative spectral densities were also observed during the full spectral density mapping of eglin *c* (Peng & Wagner, 1992b), although for fewer residues and at smaller magnitudes. However, the dynamic range issue becomes worse for larger proteins, as illustrated in Figure 2. Figure 2 shows the simplest model for the spectral density function of a protein—the single Lorentzian function for a rotating sphere—over the frequency range probed in these experiments. The solid line shows the spectral density assuming a correlation time of 4 ns, which is the approximate value for eglin *c* (8 kDa, 70 residues). The dashed line shows the spectral density assuming a correlation time of 11 ns, the approximate value for villin 14T (14 kDa, 126 residues). For the larger protein, the low-frequency components of the spectral density function (at 0 and 50 MHz) are even larger, driving the rates, especially $R_N(N_{x,y})$ and $R_{HN}(2H_zN_{x,y})$, even higher. The high-frequency components (near 500 MHz) for the larger protein are much smaller than the components for the small protein. For the larger protein, the same percent error in the rates leads to more inaccuracy in the high-frequency components. Therefore, an alternative interpretation of the motional data contained within the relaxation data, specifically one less sensitive to inaccuracies in the larger rates, is necessary for villin 14T.

Reduced Spectral Density Map for Villin 14T. The reduced spectral density map for villin 14T is shown in Figure 3. The map was calculated using the nitrogen longitudinal and transverse relaxation rates and the heteronuclear NOE enhancements under the assumption that the high-frequency components of the spectral density functions are equal [$J(\omega_H) = J(\omega_H - \omega_N) = J(\omega_H + \omega_N)$]. A reduced spectral density of this type had been suggested (Wagner, 1994; Lefévre et al., 1996) and has recently been used

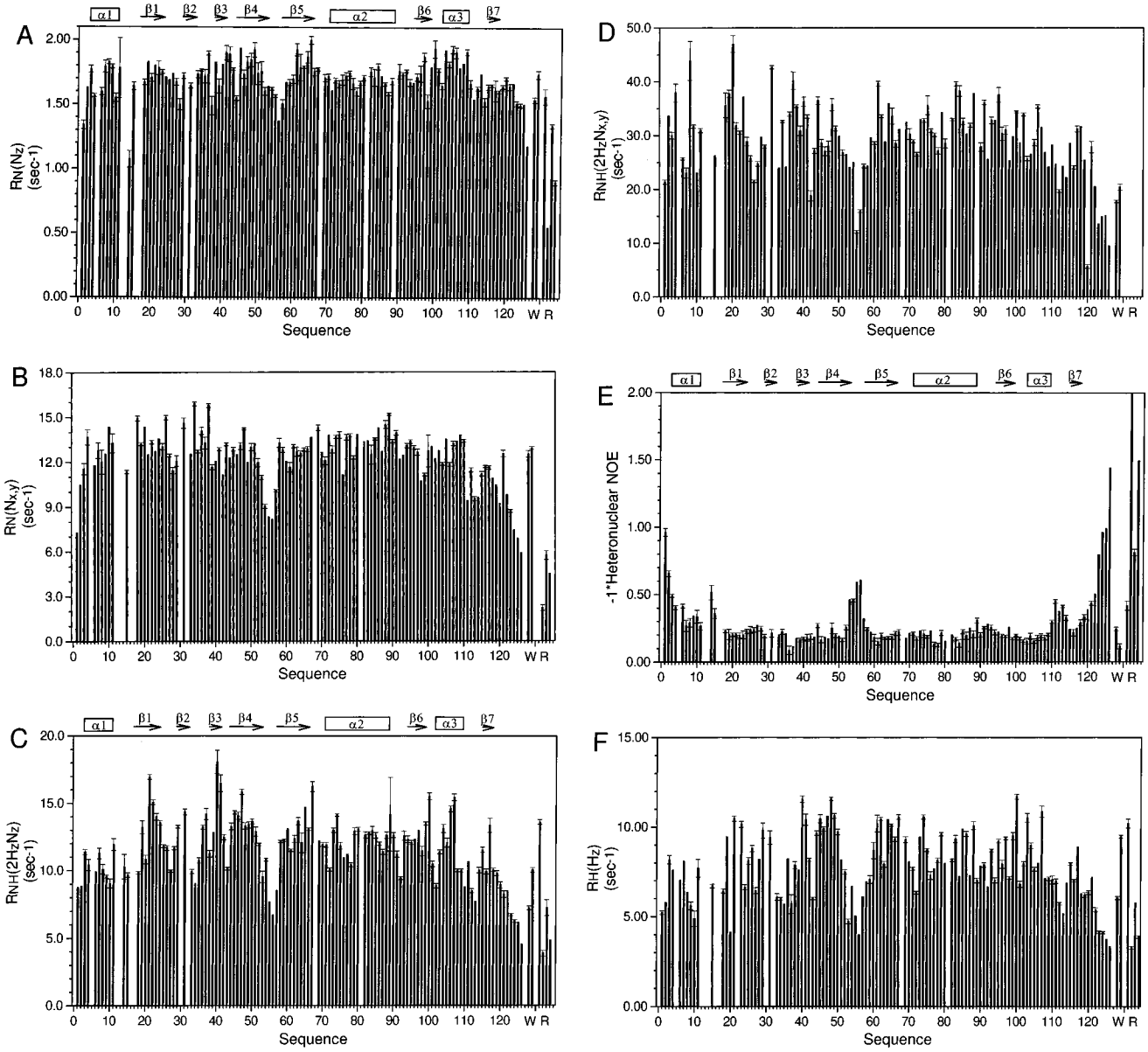

FIGURE 1: Relaxation rates and heteronuclear NOE enhancements for villin 14T measured at 500 MHz, 298 K, 2.29 mM, pH 4.13. (A) Rate for nitrogen longitudinal magnetization. (B) Rate for nitrogen transverse magnetization. (C) Rate for proton−nitrogen longitudinal two-spin order. (D) Rate for nitrogen antiphase with proton. (E) Heteronuclear NOE enhancements, displayed as magnitudes. The value off-scale on the graph is 2.3523 for the side chain of Arg^{51}. (F) Rate for proton longitudinal magnetization. The errors displayed are based on a Monte Carlo simulation for the fit; bars are not displayed for the smallest errors. The labels W and R along the sequence axis indicate the values for side-chain N−H groups, including Trp^{21}, Trp^{64}, Arg^{22}, Arg^{51}, Arg^{96}, and Arg^{107}. Rates could not be measured for prolines (Pro^{16}, Pro^{30}, and Pro^{32}) nor backbone positions lacking amide assignments (Asp^{12} and Lys^{13}). In cases of overlap, the rate is assigned to one of the two positions, typically the stronger peak, and the other is left blank. Overlapped pairs include Lys^{5} and Ala^{122}, Gly^{17} and Gly^{54}, Ile^{18} and Asn^{68}, Ser^{69} and Thr^{81}, and Gly^{89} and Gly^{120}. In some spectra, peaks for Thr^{14} are too weak to determine an accurate rate, and peaks for the Arg^{22} side chain overlap with Lys^{126}. The secondary structure is depicted above the bar graphs, with open rectangles representing α-helices and arrows representing strands of β-sheet.

in studies of an SH3 domain (Farrow et al., 1995). It has the advantage that fewer rates are required; specifically, two of the largest rates, $R_{HN}(2H_zN_{x,y})$ and $R_{HN}(2H_zN_z)$, need not be considered.

The values of $J_{eff}(0)$ along the protein backbone are shown in Figure 3A. The area under the spectral density curve is the same for each backbone amide vector within the same protein. Relatively smaller values for the spectral density at zero imply higher values at higher frequencies. Therefore, reduced values of $J_{eff}(0)$, as observed between strands β4 and β5, between helix α3 and strand β7, at the carboxyl terminus, and for arginine side chains 51, 96, and 107, are indicative of high-frequency motions. Strikingly large values of $J_{eff}(0)$, as observed for Lys^{34} and Asn^{38}, can be traced to the exchange term for the nitrogen transverse relaxation rate (eq 2). In the reduced map, the spectral density functions decrease monotonically as the frequency increases, as expected for random motion with correlation functions that decay over time (Figure 3B,C). The high-frequency component (Figure 3C) shows trends complementary to $J_{eff}(0)$, with increased spectral density between strands β4 and β5, between helix α3 and strand β7, at the carboxyl terminus, and for the arginine side chains. However, because the spectral density function spreads out when higher frequency motions are present, the increase observed at the higher frequencies is only a fraction of the decrease observed in $J_{eff}(0)$.

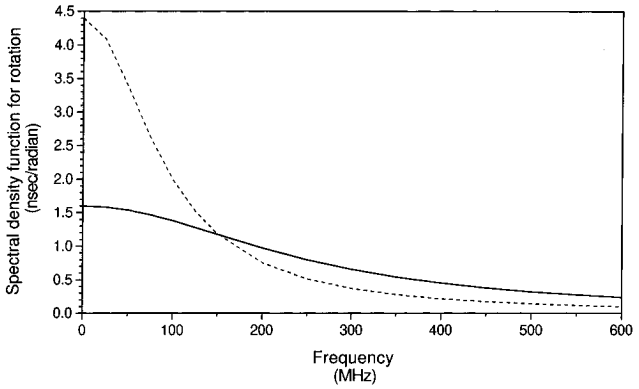

FIGURE 2: Example demonstrating the numerical problems with the full spectral density map for larger molecules. The spectral density functions for the case of an ideal rotating sphere over the frequency range sampled on a 500 MHz spectrometer are plotted. The solid line corresponds to a rotational correlation time of 4 ns, similar to the value determined for the 70-residue protein eglin *c*. The dotted line corresponds to a rotational correlation time of 11 ns, similar to the value estimated for villin 14T. For the longer correlation time, the spectral density function is much larger at low frequencies and much smaller at high frequencies. To map this spectral density from the rates, smaller differences in larger rates would have to be measured significantly.

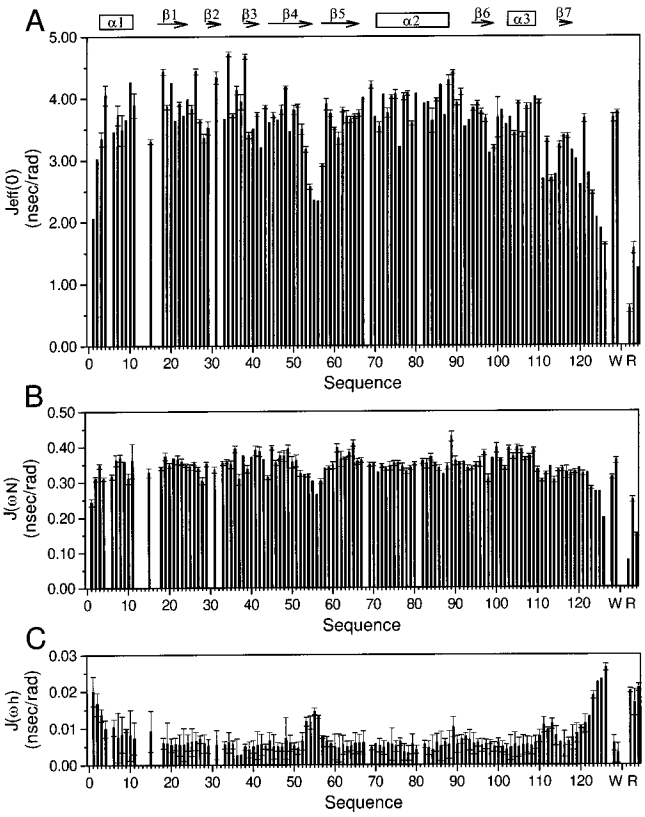

FIGURE 3: Spectral densities based on reduced fit, using the data shown in Figure 1A,B,E. (A) $J_{eff}(0)$. (B) $J(\omega_N)$. (C) $J(\omega_h) = J(\omega_H) = J(\omega_H - \omega_N) = J(\omega_H + \omega_N)$. In (B) and (C), $J(\omega_N)$ and $J(\omega_H)$ are displayed against a shortened *y*-axis to emphasize that their values are much smaller than $J_{eff}(0)$. Notice, however, that the scales in (B) and (C) are still expanded compared to (A). The RMSD for the fit is displayed as the error bars; bars are not displayed for the smallest errors. The labels W and R along the sequence axis indicate the values for side-chain N−H groups, including Trp[21], Trp[64], Arg[51], Arg[96], and Arg[107]. The secondary structure is depicted above the bar graphs, with open rectangles representing α-helices and arrows representing strands of β-sheet. This analysis corresponds perfectly to the measured rates.

The reduced spectral density functions for three representative backbone amides are plotted versus frequency in Figure 4. The dynamic range problems are obvious from this representation; the plot symbols are larger than the data values for the high-frequency components. The spectral densities for Trp[21], located in the central β-sheet, Gly[56], located in the turn between β4 and β5, and Ile[79], located in helix α2, are displayed as squares, triangles, and circles, respectively. Comparison shows that $J_{eff}(0)$ is most readily interpreted, with the low value for Gly[56] indicative of high-frequency motions. The values for Trp[21] and Ile[79] are approximately equal to the average for villin 14T, suggesting these positions mostly move with the rest of the molecule.

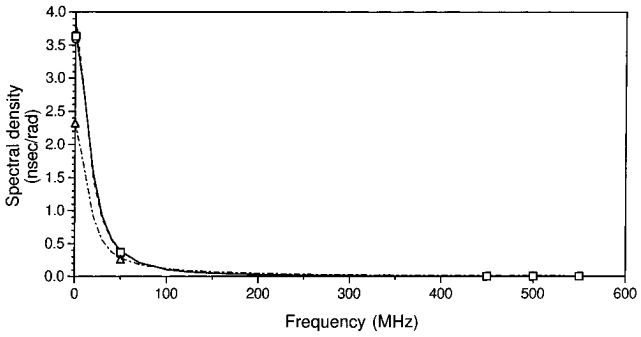

FIGURE 4: Spectral density, as mapped through the reduced fit, for representative backbone amides: squares, Trp[21], from the central β-sheet; triangles, Gly[56], from the turn between strands β4 and β5; circles, Ile[79], from helix α2. The lines through the symbols represent calculated spectral density functions based on the model-free form for Trp[21] (solid line) and Ile[79] (dashed line) and the extension including faster motions for Gly[56] (dotted-dashed line). The error bars for the values of the spectral density are similar in size or smaller than the plot symbols and are not shown. Comparison of the values for Trp[21] and Gly[56] shows significantly reduced values of $J(0)$ for the flexible turn in Gly[56]. The high-frequency components for the spectral density are twice as large for Gly[56] as for Trp[21], but the values are so small that the difference is not obvious from the figure.

Estimating Proton−Proton Contributions to Relaxation. With the estimates of the spectral density functions from the reduced map, the full map has been examined in more detail. In addition to the spectral densities, the full spectral density mapping produces a value for the proton−proton relaxation contributions ($\rho_{H^NH^i}$), which contributes to the rates $R_H(H_z^N)$, $R_{HN}(2H_zN_z)$, and $R_{HN}(2H_zN_{x,y})$. Based on the reduced map and the measured values of these rates, estimates for $\rho_{H^NH^i}$ can be calculated on the basis of eqs 6, 3, and 4. These various estimates for $\rho_{H^NH^i}$ can be compared with each other and with an estimate based on the difference between rates in deuterated and undeuterated samples (Markus et al., 1994c) to identify inconsistencies in the set of measured rates.

The estimates for $\rho_{H^NH^i}$ are shown in Figure 5. The average values, plus or minus the standard deviations, based on the rates $R_H(H_z^N)$ and $R_{HN}(2H_zN_z)$ are 7.54 ± 2.08 s^{-1} and 9.71 ± 2.40 s^{-1}, respectively, while the estimate based on $R_{HN}(2H_zN_{x,y})$ is 17.3 ± 7.2 s^{-1}. Although the estimates based on $R_H(H_z^N)$ and $R_{HN}(2H_zN_z)$ are similar, the estimate based on $R_{HN}(2H_zN_{x,y})$ is more than twice the value estimated from $R_H(H_z^N)$. The value estimated by comparison of the relaxation rate of ^{15}N labeled villin 14T with the rate for a deuterated, ^{15}N,^{13}C-labeled sample is 5.04 ± 1.84 s^{-1} (Markus et al., 1994c). This value is more similar to the estimate based on $R_H(H_z^N)$. Note that the estimate from the deuterium study is expected to be somewhat low, since the level of deuteration was approximately 80% instead of the 100% required for an accurate estimate.

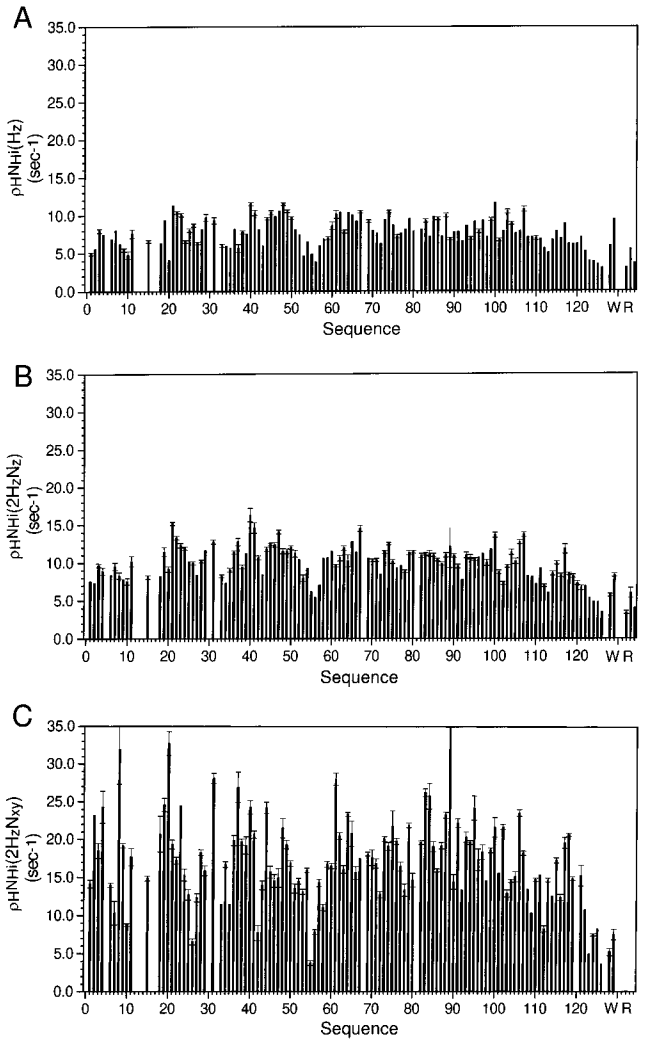

FIGURE 5: Estimates of the proton−proton contribution to the relaxation rates. (A) Estimate based on the proton longitudinal relaxation rates. (B) Estimate based on the relaxation rates for longitudinal two-spin order. (C) Estimate based on the relaxation rate for nitrogen antiphase to proton. These estimates are based on eqs 6, 3, and 4, using the values from the reduced fit for the spectral densities. The errors were derived from the Monte Carlo errors for the rates and spectral densities. The labels W and R along the sequence axis indicate the values for side-chain N−H groups, including Trp[21], Trp[64], Arg[51], Arg[96], and Arg[107].

The comparison of the estimates for $\rho_{H^NH^i}$ suggests that the antiphase relaxation rate has additional unaccounted contributions, since its $\rho_{H^NH^i}$ is strikingly higher than the others. In the full spectral density mapping, if the measured value of $R_{HN}(2H_zN_{x,y})$ is replaced with a calculated value based on the reduced spectral densities and the $\rho_{H^NH^i}$ estimated from $R_H(H^N_z)$, the $J(\omega_H)$ terms assume small positive values. $J(\omega_H)$ has the largest magnitude for the unphysical negative high-frequency density components in the full map. However, the other high frequency components remain negative. When the measured values of $R_{HN}(2H_zN_z)$ are also substituted with calculated rates, $J(\omega_H + \omega_N)$ and $J(\omega_H - \omega_N)$ assume small positive values similar to $J(\omega_H)$. Therefore, the rates $R_N(N_z)$, $R_N(N_{x,y})$, and $R_H(H_z)$, together with the heteronuclear NOE enhancements, produce reasonable values in the full spectral density map and form a consistent set of observations. Comparison of the calculated and measured values suggests that $R_{NH}(2H_zN_{x,y})$ contains errors approaching 30% while $R_{NH}(2H_zN_z)$ may have errors near 20% of its measured value. Measurement of the two-spin rates in general presents more problems than the other rates. For example, two-spin measurements show more scatter in the exponential fits for the rates. Possible sources of error include cross-correlation effects (Boyd et al., 1990; Kay et al., 1992b; Palmer et al., 1992; Peng & Wagner, 1992a) and different contributions to the proton−proton relaxation due to the different preparation of the non-amide protons during the pulse sequences. Improved measurements of two-spin relaxation rates are currently under investigation.

Model-Free Analysis. The nitrogen longitudinal and transverse relaxation rates and the heteronuclear NOE enhancements (Figure 1A,B,E) were also analyzed in the context of the model-free approach. To fit the rates and heteronuclear NOE enhancements to the model-free formalism, an estimate of the overall correlation time for tumbling, τ_m, is required for the grid search to converge. The overall correlation time can be estimated from the ratio of the rates $R_N(N_z)$ (eq 1) and $R_N(N_{x,y})$ (eq 2) by neglecting the exchange contribution and assuming the model-free form for the spectral density functions (eq 14) (Kay et al., 1989). Only ratios within one standard deviation of the mean are considered initially to eliminate amide groups which require more extended models for fitting. This approximation gives a value of 9.3 ns over 95 amide groups. Reducing the number of groups considered further, to the 60 with ratios closest to the mean, did not change the estimate significantly. During the grid search, the molecular correlation time is optimized. Optimization drove the value to 10.5 ± 0.2 ns. When the model-free approach was proposed, the authors pointed out that the fit for S^2 and τ_e is not very sensitive to the value chosen for τ_m (Lipari & Szabo, 1982b). However, since τ_m has immediate intuitive meaning, it is often quoted as a result in relaxation studies of proteins. The range of values calculated for villin 14T (9.3−10.5 ns) points to the danger of ascribing too much significance to the precise value of this parameter.

With a value for τ_m, S^2 and τ_e are optimized until the input data are satisfactorily fit on the basis of spectral densities of the form in eq 14. A satisfactory fit was taken to be one that reproduced the rates to within 10% of their experimental values and the heteronuclear NOE enhancements to 20% of their experimental values. The data for 72 out of 128 amide groups could be fit with the original model-free formalism by this criterion. Data for 35 more amide groups could be fit with the extension of the model free formalism that considers fast motions on two separable time scales, described in eq 15. Data for 7 more could be fit with the form of the spectral density function from eq 14 plus explicit consideration of the exchange contribution to $R_N(N_{x,y})$. When the acceptance criterion for the heteronuclear NOE enhancement was relaxed to agreement between calculation and experiment to 80%, data for 1 more residue could be fit with the original model-free approach, data for 7 more residues could be fit with the extended model-free approach and data for 3 more with an explicit exchange term. Data for 3 residues were not fit well by any of the three approaches. Representative fits are shown for the backbone amides of Trp[21], Gly[56], and Ile[79] by the curves in Figure 4. The results for all $^1H-^{15}N$ groups are summarized in Table 1, provided in the supporting information.

For many of the amide groups, τ_e was optimized to a value approaching or exceeding τ_m. Although these values reproduce the measured rates, the interpretation of the model-free approach is based on the assumption that motions slower

than the overall tumbling will be averaged out, leaving only fast internal motions. The model-free parameters are only reasonably accurate for $\omega\tau_e < 0.5$ and $S^2 > 0.01$ (Lipari & Szabo, 1982a). The large values of τ_e for some residues in villin 14T suggest that the time scale for internal motions is not sufficiently distinct from the overall tumbling to be fit accurately. Considering only values of S^2 for amide groups with $\tau_e < 10$ ns, the average value is 0.80, in line with values for staphylococcal nuclease (Kay et al., 1989) and interleukin 1β (Clore et al., 1990b). The range is from 0.131 to 0.999. Significantly lower order parameters are observed for the turn between strands β4 and β5, the turn between α3 and strand β7, at the carboxyl terminus, and for the arginine side chains, consistent with the trends observed in the rates.

The model-free approach is based on the assumption of isotropic tumbling by the protein, described by one correlation time. However, on the basis of the structure of villin 14T, the ratio of the principal moments of inertia of the domain is 1.73:1.55:1.00. One overall correlation time has proven sufficient for other globular but not spherical proteins, such as staphylococcal nuclease (moments of inertia ratio 1.39:1.31:1.00; Kay et al., 1989) and HIV-1 protease (considered an oblate ellipsoid with axis ratio 1.6:1.0; Nicholson et al., 1995). It remains to be seen if explicit consideration of the shape of villin 14T, known from structural studies (Markus et al., 1994a), would produce more reasonable values for τ_e in the model-free formalism.

$R_H(H_{\rho z})$ as a Function of Spin-Locking Field Strength To Examine Exchange Contributions. An estimate of the exchange contribution to $R_N(N_{x,y})$ can be obtained from an extension of the model-free approach, described above. Exchange processes can also be studied directly by examining the dependence of $R_X(X_{\rho z})$ on the spin-locking field strength (Deverell et al., 1970; Szyperski et al., 1993). For typical spin-locking fields in the kilohertz range, processes on the microsecond to millisecond time scales can be examined. To extend the information from the nitrogen relaxation rates, we measured the transverse rates for amide protons as a function of spin-locking field strength. For most of the amide groups, the rate was independent of the spin-locking field over the range of field strengths explored. On the basis of eq 16, the null result can be due to the absence of exchange processes on this time scale or the lack of a significant chemical shift difference between the exchanging states. For Thr^8, there was some dependence on the spin-locking field strength, but the peak is too broad and weak to significantly estimate a time constant for exchange.

The most striking results, for Leu^{11}, are shown in Figure 6. On the basis of a Levenburg−Marquardt fit to eq 16, the exchange time constant for Leu^{11} is 125 ± 69 μs. Experimental observation of an exchange process acting at Leu^{11} is consistent with Leu^{11}'s appearance as a broad, weak peak in ^{15}N HSQC spectra. Furthermore, peaks for the adjacent residues Asp^{12} and Lys^{13} have not been observed in any of our ^{15}N heteronuclear correlation spectra so far; it is possible that the exchange process observed through Leu^{11} broadens these peaks beyond detection. The backbone positions with evidence for slow conformational exchange, as well as the positions with missing amide assignments, are indicated on the structure in Figure 7A. This evidence for slow conformational exchange in the hinge joining helix α1 to the rest of the protein reopens the question of the source of pairs of peaks for certain residues (Markus et al., 1994b). Pairs of peaks have been observed for residues in helix α1 (Leu^3, Ser^4, Lys^5, Val^7, Thr^8, Lys^{10}, and Leu^{11}) and residues in helix α2 facing helix α1 (Tyr^{80}, Thr^{81}, and Met^{84}). Since the sample contains protein molecules with and without the initiator methionine residue, the presence of two types of molecule has been offered as a possible explanation for two sets of peaks (Markus et al., 1994b). However, a slow conformational exchange between two orientations within individual molecules is another possible explanation, consistent with slow exchange at Leu^{11}. So far, the pattern of NOE cross peaks for both forms is similar, suggesting that the structures are similar. Therefore, a putative conformational exchange would likely involve a small reorientation of helix α1.

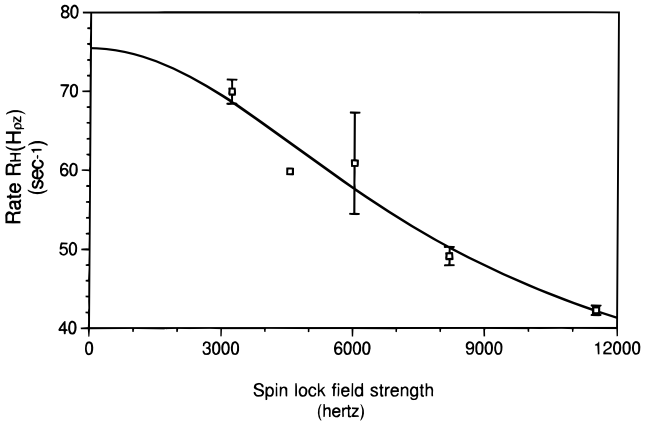

FIGURE 6: Rate $R_H(H_{\rho z})$ as a function of spin lock for Leu^{11}. The rates, measured at five different spin-locking field strengths, are plotted as boxes. Error bars show the estimate based on 500 Monte Carlo simulations of the rate calculations. The solid line shows the best fit curve, based on eq 16 fit by the Levenburg−Marquardt algorithm. The time constant for the exchange process reflected in the rate's dependence on field strength is 125 ± 69 μs.

DISCUSSION

For villin 14T, the best formalism for analyzing the rates is apparently the reduced spectral density map. The reduced spectral density map has the same advantages as the full spectral density map—there are no *a priori* assumptions about the motions in the system. The motional data can be extracted from the rates without regard to model, making it available to test the validity of different models. In exchange for one assumption—that the spectral density function at high frequencies is small enough that $J(\omega_H)$, $J(\omega_H - \omega_N)$, and $J(\omega_H + \omega_N)$ can be set equal—the reduced spectral density map requires only three measurements. For example, in this study the reduced spectral densities have been calculated from nitrogen longitudinal and transverse relaxation rates and the heteronuclear NOE enhancements. Inaccuracies in the measurement of two-spin relaxation rates, especially R_{NH}-$(2H_zN_{x,y})$, are not a problem for the reduced spectral density map.

On the basis of the rates themselves, the model-free order parameter, and the zero-frequency component of the spectral density function, the same trends in mobility along the backbone of villin 14T emerge. For high-frequency motions, the spectral density functions report most directly. High frequency, at the field strength used for these experiments, is approximately 500 MHz. This translates into a time scale for motion on the order of nanoseconds. Motions faster than any overall tumbling will also be sampled, into the picosecond time scale. For low-frequency motions, conforma-

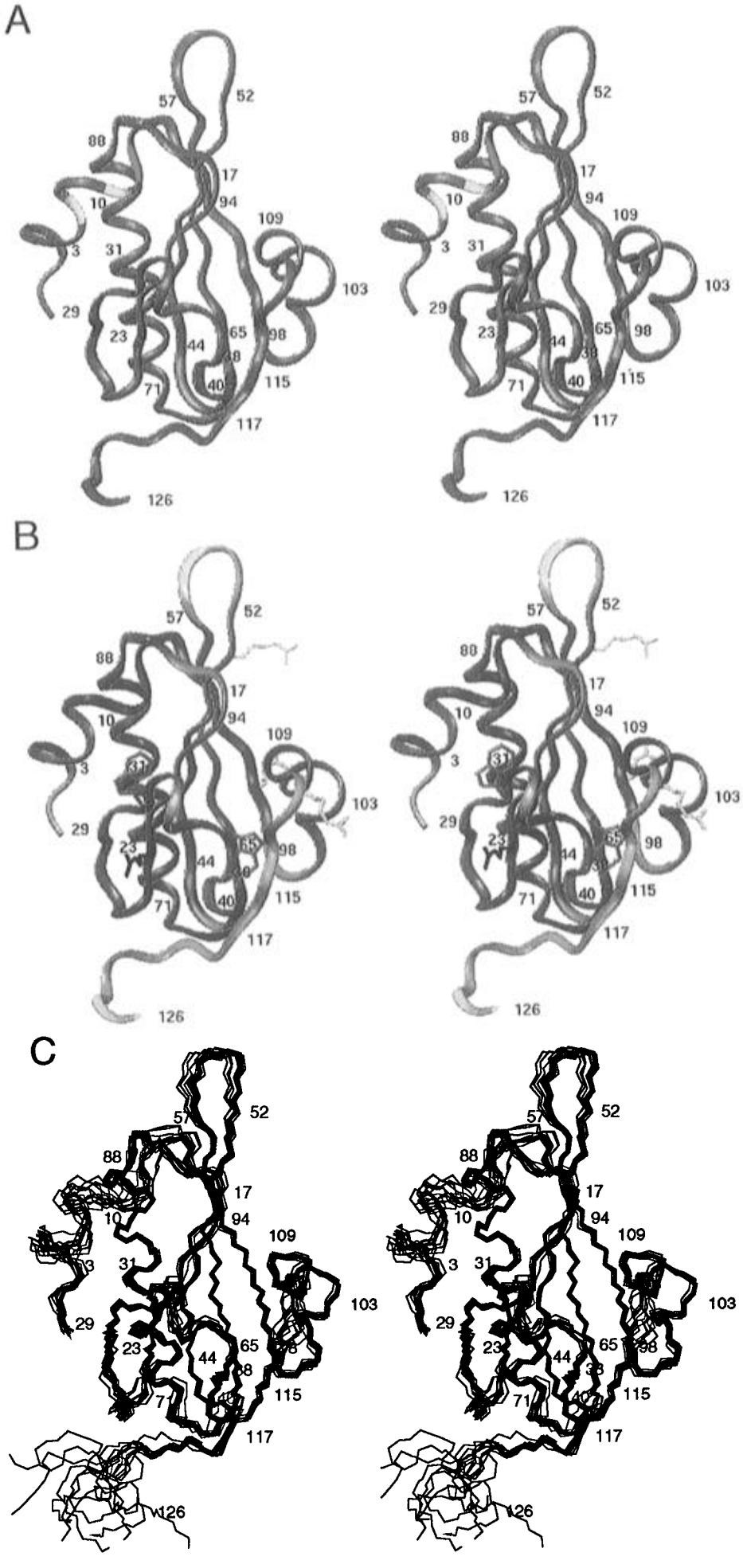
A
B
C
57
52
88
17
10
94
109
3
31
103
29
23
65
98
44
38
115
71
40
117
126

FIGURE 7: Defocused stereo representations of the backbone ribbon of villin 14T. (A) Backbone positions involved in slow conformational exchange, based on $R_H(H_{pz})$ as a function of spin lock. The base color for the ribbon representation of villin 14T is blue. Thr[8] and Leu[11], which show a dependence on spin-lock field strength, are color-coded yellow. Asp[12] and Lys[13], which lack backbone amide assignments, are shown in red. (B) The pattern of mobility inferred from the transverse relaxation rates for backbone amide nitrogen nuclei [$R_N(N_{x,y})$]. For positions with rates near the average value, the ribbon is colored blue. For positions with rates above the mean, the ribbon becomes dark blue, pink, and then white as the rate increases to one, two, and three standard deviations above the mean. For positions with rates below the mean, the ribbon becomes light blue, green, and then yellow as the rate decreases to one, two, and three standard deviations below the mean. High rates [purple, pink, and white (not seen)] are indicative of exchange processes and reflect motion on the microsecond to millisecond time scale. Low rates (blue-green, green, yellow) reflect fast motions, on the picosecond to nanosecond time scale. The side chains for Trp[21], Trp[64], Arg[51], Arg[96], and Arg[107], whose mobility is also probed in nitrogen relaxation measurements, are shown and color-coded appropriately. For Arg[22], the nitrogen transverse relaxation rate could not be measured due to overlap, so the side chain is shown in black to identify its location. (C) Bundle of 12 distance geometry structures, calculated using a revised and expanded restraint list, including 1321 NOE restraints. The regions with the most variation in the bundle of structures correspond qualitatively to the regions with evidence of mobility in (A) and (B). In all three panels, numbers indicate end points of elements of regular secondary structure and serve as references. This figure was generated with InsightII from Biosym Technologies, San Diego, CA.

tional exchange (R_{ex}^N, R_{ex}^H) reports most directly. Measurements of R_{ex}^N or R_{ex}^H through spin-locking experiments probe motions on the microsecond to millisecond time scale.

One rate has large contributions from both $J(0)$ and R_{ex}^N—the nitrogen transverse relaxation rate [$R_N(N_{x,y})$]. To summarize the patterns of mobility in villin 14T, this rate has been used to color-code the structure in Figure 7B. Residues with large values of $R_N(N_{x,y})$, indicative of exchange, are color-coded dark pink to white in Figure 7B. Note that none of the backbone positions appear white because none of the rates are more than two standard deviations above the mean. Conformational exchange occurs between strands β1 and β2 and between strands β2 and β3. Residues with small values of $R_N(N_{x,y})$, indicative of small $J(0)$ and therefore high frequency motions, are color-coded green to yellow in Figure 7B. Fast motions occur at the amino terminus, between strands β4 and β5, between helix α3 and strand β7, and at the carboxyl terminus. In general, mobility is evident in turns on the surface of the domain. The hydrophobic core of villin 14T shows relatively uniform relaxation rates, suggesting uniform motions. These trends in mobility correlate qualitatively with the regions of highest RMSD per residue for the ensemble of 12 distance geometry structures calculated for villin 14T, shown in Figure 7C (Markus et al., 1994a).

^{15}N relaxation measurements also provide information about mobility at tryptophan and arginine side-chain positions, shown in Figure 7B. Trp[21] and Trp[64] are on opposite sides of the central β-sheet. Trp[64] is strongly conserved among all actin severing domains and packs into hydrophobic residues in helix α3. Trp[21] is only conserved among the actin-monomer binding domains, found at repeats 1 and 4 within the actin severing proteins. It interacts with side chains from helices α1 and α2 to form the hydrophobic core on the other side of the sheet. Both tryptophan side chains show relaxation rates close to the average for the measured positions, suggesting that in general they move with the core of the protein. Trp[21] consistently shows lower rates and higher heteronuclear NOE enhancements than Trp[64], suggesting that it might be slightly more mobile. This is consistent with the observation that Trp[21] has slightly more solvent-accessible surface and shows more variability in solvent-accessible surface over an ensemble of distance geometry structures than Trp[64] (5.0 ± 3.7 Å^2 versus 1.8 ± 1.2 Å^2). As for the arginine side chains, rates and heteronuclear NOE enhancements for Arg[22] are more similar to the core of the protein while rates and heteronuclear NOE for the others (Arg[51], Arg[96], and Arg[107]) follow the trends for the unrestrained termini, sometimes suggesting even more mobility. Arg[22] is more buried than the other arginine side chains, with a solvent-accessible surface area over an ensemble of 12 distance geometry structures of 68 ± 16 Å^2 versus 154 ± 14, 160 ± 16, and 141 ± 12 Å^2 for the others. Arg[22] and Arg[96] are conserved among actin-monomer binding repeats 1 and 4. Arg[22] participates somewhat in the hydrophobic core between the central β-sheet and the small parallel β-sheet. The analog of Arg[96] in gelsolin segment 1 makes a hydrogen bond to actin in the complex (McLaughlin et al., 1993).

Relating Mobility to Function. Do the patterns of mobility correlate with regions involved in functions of this domain? For example, an empty binding site might be expected to be more flexible than the rest of the protein, as seen for the calcium-binding protein, calbindin D_{9k} (Akke et al., 1993). This flexibility could contribute to the fit with ligand, since the cost of the entropy loss upon binding would be offset by favorable energetic interactions. There are two calcium-binding sites within villin 14T. At the weaker calcium-binding site, ligands are most likely provided by the side chain of Asp[85] and the backbone carbonyls of Ser[90] and Ala[92], with missing ligands from actin (McLaughlin et al., 1993; Markus et al., 1994a). These residues are located at the carboxyl terminus of helix α2. These residues show little evidence for local backbone motion, suggesting a preformed calcium-binding site. The stronger calcium-binding site involves side chains from Asp[43] and Glu[73] as well as backbone carbonyls from Gly[42] and Val[121], based on comparison with gelsolin and calcium titration experiments (McLaughlin et al., 1993; Markus et al., 1994a). Val[121] shows evidence of high-frequency motions. Although it is not clear if this mobility is functionally important or an artifact of truncating the domain, calcium-dependent reorganization at the carboxyl terminus of the domain would influence the orientation of the first domain relative to the second domain and could provide a mechanism for calcium regulation of the actin-binding activity. Different cleavage patterns between domains have been observed in the presence or absence of calcium for villin (Bazari et al., 1988). One caution for interpretation of the mobility in the calcium-binding sites is that the NMR studies have been done at pH 4.15. Judged by ^{15}N HSQC spectra, the low pH form of the protein resembles the calcium-loaded form, and the related protein, gelsolin, binds to actin with similar affinity whether at low pH without calcium or at higher pH with calcium (Lamb et al., 1993). Another caveat for interpretation of the relaxation data is that additional mobility may be present at time scales other than those probed by NMR (picoseconds to nanoseconds and microseconds to milliseconds).

Villin 14T also binds to actin monomers. On the basis of the cocrystal structure of gelsolin segment 1 (McLaughlin

et al., 1993), residues corresponding to Leu[3], Ser[4], Met[26], Glu[27], Tyr[63], Gln[71], Ile[79], Thr[82], Gln[83], Glu[86], Gln[94], Arg[96], and Met[125] in villin 14T participate in either hydrophobic interactions or hydrogen bonds with actin. Residues 71−88 form helix α2, which shows rates and heteronuclear NOE enhancements consistent with the core of the molecule. Evidence for motions in the actin-contact residues includes high values of $R_N(N_{x,y})$ for Met[26], indicative of some slow motions at that position, and low values of $R_N(N_{x,y})$ for Met[125] and the Arg[96] side chain, implying fast motions at these positions. Fast motions for Met[125] at the end of the peptide chain may be an artifact of the isolated domain in solution. Overall, the lack of motion along the actin-binding site indicates that the site is preformed, complementary to actin even when the domain is free in solution. The nanosecond to picosecond mobility in the side chain for Arg[96] suggests that side-chain adjustments are important for interaction. Recent developments in relaxation measurement using ^{13}C (Yamazaki et al., 1994) hold promise that techniques will be developed to measure mobility at additional side-chain positions.

^{15}N and ^{1}H relaxation measurements provide a better understanding of the dynamic actin-severing domain, villin 14T, alone in solution. More detailed understanding of the importance of mobility for function will come with additional studies on mobility in complexes of villin 14T with calcium and possibly actin or actin peptides.

ACKNOWLEDGMENT

The authors thank Drs. Jeffrey Peng and Elizabeth Meiering for helpful discussions during the course of these studies. The authors are indebted to Dr. Peng for providing his analysis programs. M.A.M. thanks Dr. Lewis Kay for emphasizing the importance of proton−proton contributions to amide proton relaxation.

SUPPORTING INFORMATION AVAILABLE

Table 1, which gives the order parameters and time constants for the model-free fit for the measured relaxation rates (4 pages). Ordering information is given on any current masthead page.

REFERENCES

Abragam, A. (1961) *The Principles of Nuclear Magnetism*. Chapter VIII. Clarendon Press, Oxford.
Akke, M., Skelton, N. J., Kördel, J., Palmer, A. G., III, & Chazin, W. J. (1993) *Biochemistry 32*, 9832−9844.
Bazari, W. L., Matsudaira, P., Wallek, M., Smeal, T., Jakes, R., & Ashmed, Y. (1988) *Proc. Natl. Acad. Sci. U.S.A. 85*, 4986−4990.
Blackledge, M. J., Brüschweiler, R., Griesinger, C., Schmidt, J. M., Ping Xu, & Ernst, R. R. (1993) *Biochemistry 32*, 10960−10974.
Bloch, F. (1946) *Phys. Rev. 70*, 460−474.
Bloembergen, N., Purcell, E. M., & Pound, R. V. (1948) *Phys. Rev. 73*, 679−718.
Boyd, J., Hommel, U., & Campbell, I. D. (1990) *Chem. Phys. Lett. 175*, 477−482.
Clore, G. M., Szabo, A., Bax, A., Kay, L. E., Driscoll, P. C., & Gronenborn, A. M. (1990a) *J. Am. Chem. Soc. 112*, 4989−4991.
Clore, G. M., Driscoll, P. C., Wingfield, P. T., & Gronenborn, A. M. (1990b) *Biochemistry 29*, 7387−7401.
Davis, A. L., Keeler, J., Laue, E. D., & Moskau, D. (1992) *J. Magn. Reson. 98*, 207−216.
Dayie, K. T., & Wagner, G. (1994) *J. Magn. Reson. A 111*, 121−126.
Deverell, C., Morgan, R. E., & Strange, J. H. (1970) *Mol. Phys. 18*, 533−559.
Farrow, N. A., Zhang, O., Forman-Kay, J. D., & Kay, L. E. (1995) *Biochemistry 34*, 868−878.
Grzesiek, S., & Bax, A. (1993) *J. Am. Chem. Soc. 115*, 12593−12594.
Janmey, P. A., & Matsudaira, P. T. (1988) *J. Biol. Chem. 263*, 16738−16743.
Kay, L. E., Torchia, D., & Bax, A. (1989) *Biochemistry 28*, 8972−8979.
Kay, L. E., Keifer, P., & Saarinen, T. (1992a) *J. Am. Chem. Soc. 114*, 10663−10665.
Kay, L. E., Nicholson, L. K., Delaglio, F., Bax, A., & Torchia, D. A. (1992b) *J. Magn. Reson. 97*, 359−375.
Lamb, J. A., Allen, P. G., Tuan, B. Y., & Janmey, P. A. (1993) *J. Biol. Chem. 268*, 8999−9004.
Lefévre, J. F., Dayie, K. T., Peng, J. W., & Wagner, G. (1996) *Biochemistry* (in press).
Lipari, G., & Szabo, A. (1982a) *J. Am. Chem. Soc. 104*, 4546−4559.
Lipari, G., & Szabo, A. (1982b) *J. Am. Chem. Soc. 104*, 4559−4570.
Markus, M. A., Nakayama, T., Matsudaira, P., & Wagner, G. (1994a) *Protein Sci. 3*, 70−81.
Markus, M. A., Nakayama, T., Matsudaira, P., & Wagner, G. (1994b) *J. Biomol. NMR 4*, 553−574.
Markus, M. A., Dayie, K. T., Matsudaira, P., & Wagner, G. (1994c) *J. Magn. Reson. B 105*, 192−195.
McLaughlin, P. J., Gooch, J. T., Mannherz, H.-G., & Weeds, A. G. (1993) *Nature 364*, 685−692.
Nicholson, L. K., Yamazaki, T., Torchia, D. A., Grzesiek, S., Bax, A., Stahl, S. J., Kaufman, J. D., Wingfield, P. T., Lam, P. Y. S., Jadhav, P. K., Hodge, C. N., Domaille, P. J., & Chang, C.-H. (1995) *Nature Struct. Biol. 2*, 274−280.
Nirmala, N. R., & Wagner, G. (1988) *J. Am. Chem. Soc. 110*, 7557−7558.
Nirmala, N. R., & Wagner, G. (1989) *J. Magn. Reson. 82*, 659−661.
Palmer, A. G., III, Cavanagh, J., Wright, P. E., & Rance, M. (1991) *J. Magn. Reson. 93*, 151−170.
Palmer, A. G., III, Skelton, N. J., Chazin, W. J., Wright, P. E., & Rance, M. (1992) *Mol. Phys. 75*, 699−711.
Peng, J. W., & Wagner, G. (1992a) *J. Magn. Reson. 98*, 308−332.
Peng, J. W., & Wagner, G. (1992b) *Biochemistry 31*, 8571−8586.
Peng, J. W., Thanabal, V., & Wagner, G. (1991) *J. Magn. Reson. 95*, 421−427.
Redfield, A. G. (1965) *Adv. Magn. Reson. 1*, 1−32.
Sklenár, V., Torchia, D., & Bax, A. (1987) *J. Magn. Reson. 73*, 375−379.
Szyperski, T., Luginbühl, P., Otting, G., Güntert, P., & Wüthrich, K. (1993) *J. Biomol. NMR 3*, 151−164.
Wagner, G. (1993) *Curr. Opin. Struct. Biol. 3*, 748−754.
Wagner, G. (1994) *Approaches for Studies of Protein Mobility and Structure*, The 35th Experimental Nuclear Magnetic Resonance Conference, April 10−15, 1994, Asilomar, CA.
Yamazaki, T., Muhandiram, R., & Kay, L. E. (1994) *J. Am. Chem. Soc. 116*, 8266−8278.

BI951933O